Planetary and Space Science 181 (2020) 104787

Contents lists available at ScienceDirect

Planetary and Space Science

journal homepage: www.elsevier.com/locate/pss

Evaluation of the bandwidths and spatial resolutions achievable with near-infrared observations of Venus below the cloud deck

J. Knicely [a,*], R.R. Herrick [a]

[a] Geophysical Institute, University of Alaska Fairbanks, 2156 N Koyukuk Dr, Fairbanks, AK, 99775, USA

ARTICLE INFO

Keywords:
Venus
Surface viewing atmospheric windows
Spectroscopy
Balloon
Aerial vehicle

ABSTRACT

We identified potential atmospheric windows with which to study the Venusian surface on the nightside and calculated the approximate scattering footprint as would be seen by a prospective aerial mission. The emission from the surface, its scattering through the atmosphere, and the emission from the atmosphere were calculated from the surface to various heights beneath the cloud deck. We explored the effects of different sensor altitudes, varying surface emissivity, variation in elevation causing changes in surface temperature, and variations in the temperature profile, on the possible surface viewing atmospheric windows. The effects of surface emissivity and surface elevation dominated, and those of sensor altitude and variation in temperature profile are relatively small. The prospective windows are largely expanded versions of previously identified windows that have been exploited by satellites and ground-based observation with an additional window centered at 1.27 μm. Any mission that exploits the improved visibility beneath the cloud decks should make use of 0.7–1.0, 1.1, and 1.27 μm windows, as these provide a comprehensive ability to extract information about the surface. We explored the effect of sensor altitude and surface elevation on the scattering footprint. The scattering footprint beneath the cloud deck varies from ~15 to 5 km depending on wavelength at our nominal altitude of 40 km, a significant improvement over the 50–100 km footprint for orbiting satellites. Lowering the sensor altitude only mildly reduces the scattering footprint, as most scattering is caused by the dense lowermost atmosphere. Increased surface elevation reduces the scattering footprint. We concluded that regions elevated above the mean planetary radius represent the best targets as these have the greatest amount of the electromagnetic spectrum identified as surface viewing atmospheric windows and the smallest scattering footprint. These windows have the potential to elucidate questions about the composition and redox state of the surface of Venus, even for low emissivity materials (e.g., fine-grained hematite at ε~0.5), which have important implications for the evolution of the planet.

1. Introduction

The study of the Venusian surface is an arduous task. Surface probes have been short-lived (on the order of hours) due to the harsh surface conditions (~735 K and ~92 bars) (e.g., Seiff et al., 1985; Crisp and Titov, 1997) and sulfuric acid (Bezard and de Bergh, 2007), requiring other means for any long-term or comprehensive study of the surface. Generally, that involves the use of orbiting satellites or ground-based telescopes. With Venus, we also have the option of using balloons or other aerial systems, which can remain just beneath the cloud deck where temperature and pressure conditions are similar to Earth surface conditions (Moroz, 2002). Surface viewing atmospheric windows are now well-identified for systems above the cloud deck, but atmospheric windows at lower altitudes, such as for a balloon, are not well constrained. Moroz (2002) examined possible windows at 0.65, 0.85, and 1.02 μm through which emission from the surface on the nightside of Venus could reach a sensor at altitude. The present work seeks to expand on Moroz (2002) by modeling the surface emission of bands from 0.7 to 250 μm using a total extinction coefficient data set from Lebonnois et al. (2015). Spectroscopic study of the surface of Venus using near-infrared (NIR) wavelengths such as these has the potential to unravel crucial portions of the Venusian history by revealing the composition of the surface, the history of water, and by helping to identify stratigraphic relationships (Baines et al., 2000; Hashimoto et al., 2008; Mueller et al., 2008; Kappel et al., 2016). The emission from the surface, its scattering through the atmosphere, and the emission from the atmosphere were calculated from the surface to various heights beneath the cloud deck. We explored the effects of different sensor altitudes, various surface

* Corresponding author. Geophysical Institute, 2156 N Koyukuk Dr, Fairbanks, AK, 99775, USA.
E-mail address: jknicely@alaska.edu (J. Knicely).

https://doi.org/10.1016/j.pss.2019.104787
Received 27 June 2019; Received in revised form 5 October 2019; Accepted 1 November 2019
Available online 3 November 2019
0032-0633/

emissivities, variation in elevation causing changes in surface temperature (and pressure), and variations in the temperature profile on the possible atmospheric windows. Following this, we calculated the scattering footprint for different sensor altitudes and surface elevations using a method from Ashikhmin et al. (2004). The potential uses and caveats of these surface viewing windows and scattering footprints are then discussed.

2. Background

Carbon dioxide and molecular nitrogen constitute the bulk of the lower atmosphere of Venus at 96.5% and 3.5% respectively (Taylor et al., 1997; Bezard and de Bergh, 2007). A small portion of the atmosphere is composed of noble gases (most notably argon) and a number of chemically active species on the order of several thousandths to several thousand parts per million including H_2O, CO, OCS, SO_2, HCl, and HF (Taylor et al., 1997; Bezard and de Bergh, 2007; Arney et al., 2014). These gases combine to create a surface pressure of ~92 bar (Seiff et al., 1985; Lebonnois et al., 2015). At such high pressures, molecular collisions distort the shape of the colliding molecules and drastically broaden the absorption bands (Taylor et al., 1997; Lebonnois et al., 2015; Rothman et al., 2010). Until 1990, surface studies were believed relegated to radar wavelengths (Baines et al., 2000) in part due to inaccuracies in previous collision-induced absorption predictions (Taylor et al., 1997). While useful, these wavelengths are limited in the compositional information they can provide. Landers obtained imagery in the visible and one NIR band, but these data are localized and have large errors (Pieters et al., 1986). Following the *Galileo* flyby of Venus in 1990, several atmospheric windows were confirmed in the near- and mid-infrared bands (0.85, 0.9, 1.01, 1.10, and 1.14–1.19 μm) that allowed viewing of the surface of Venus on the nightside of the planet (Allen and Crawford, 1984; Carlson et al., 1991; Crisp et al., 1991; Crisp and Titov, 1997; Baines et al., 2000; Hashimoto et al., 2008; Peralta et al., 2017; Helbert et al., 2018; Taylor et al., 1997). Viewing of the surface from orbit is only possible on the nightside of the planet because scattering of sunlight overwhelms any surface signature on the dayside, often by as much as 3 orders of magnitude (Kappel et al., 2016; Titov et al., 2007).

Of great interest is the composition of the surface. Chemical data obtained suggests mafic composition (Treiman, 2007), as does visual data from probes to the surface (Pieters et al., 1986). Problematically, this data is of poor precision (Hashimoto et al., 2008), is relevant only for a local region, and does little to elucidate the true composition of the surface, as ultra-mafic, intermediate, and even some felsic rocks fit the current data constraints (Treiman, 2007; Kappel et al., 2016). Precise and accurate surface composition data would provide a key clue in answering questions about the history of the surface of Venus: has plate tectonics operated on its surface? How much water, if any, did Venus have in the past? Determination of broad rock types in Venusian conditions is being pioneered by the German Institute for Planetary Research (DLR) (Helbert et al., 2017, 2018). At this facility, the emissivities of felsic and mafic rocks have been and continue to be measured at the elevated surface temperatures of Venus (pressure has little to no influence on emissivity) (Helbert et al., 2017). A partial database is complete and further additions will provide useful constraints on the wavelength dependent emissivity of various materials at Venusian conditions. Their work has shown that general rock composition (e.g., felsic versus mafic) and identification of minerals associated with weathering can be identified on Venus from surface emissivity in the 0.7–1.5 μm wavelength range.

3. Methods

We explored the effects of sensor altitude, emissivity, variation in elevation causing changes in surface temperature, and variations in the temperature profile on the possible atmospheric windows. Sensor altitude varied in 10 km intervals from 10 to 100 km, though we concentrated on sensor altitudes of 50 km or below for reasons stated further below. Emissivity values were unity (1.0), 0.95, 0.86, and 0.7. The 2 higher values were used to simulate more mafic materials and the 2 lower more felsic (Jensen, 2007; Lillesand et al., 2015). Emissivity is wavelength dependent and can also be affected by other variables not included here (e.g., grain size, surface roughness, layers of regolith, temperature) (e.g., Gilmore et al., 2015; Jensen, 2007; Haus and Arnold, 2010). Common felsic and mafic materials, such as rhyolite and basalt, have a similar emissivity of ~0.88 at wavelengths of 0.85 μm. The two diverge with increasing wavelength: felsic materials dip to ~0.86 at 0.9 μm, rise to ~0.90 at 1.0 μm, and then rise to ~0.93 at 1.18 μm; mafic materials rise to ~0.9 at 0.90 μm, and then plateau at ~0.97 for wavelengths of 1.0–1.18 μm (Helbert et al., 2017, 2018). Bright felsic materials, such as anorthosite, tend to have a nearly featureless, flat spectra (Kappel et al., 2016; Helbert et al., 2017). Bulk values of emissivity were chosen and are largely similar to measured values of similar rock types at Venusian temperatures (e.g., Helbert et al., 2018). Modeled surface elevations were 0 and 11 km, with surface temperatures of 735 and 650 K respectively. The temperature profile of Seiff et al. (1985) was used with 20 K added, and then with 20 K subtracted, from both the surface temperature and temperature at all altitudes to simulate changes in the temperature profile that may occur at different latitudes and regions (Haus and Arnold, 2010). Our nominal conditions were a surface elevation of 0 km, a sensor altitude of 40 km, a surface temperature of 735 K, the temperature profile from Seiff et al. (1985), and an emissivity of unity (1). The nominal surface temperature used is the average of 735K*K*, though the temperature profile can vary by as much as several tens of kelvin depending on altitude (Seiff et al., 1985; Crisp and Titov, 1997; Hashimoto et al., 2008; Mueller et al., 2008) and the surface temperature of the lowest altitude (−2 km) compared to the highest altitude locations (11 km) can be 100 K warmer (Haus and Arnold, 2010).

We calculated the surface signal using the Planck blackbody function modified by the assumed emissivity of the material:

$$I(\lambda) = \varepsilon B_{surface}(\lambda, T) = \varepsilon \frac{2hc^2}{\lambda^5} \frac{1}{exp\left[\frac{hc}{\lambda k_B T}\right] - 1} \tag{1}$$

where ε is the emissivity, λ is the wavelength in meters, T is temperature in kelvin, h the Planck constant ($6.62 \times 10^{-34} Js$), c is the speed of light ($2.9979 \times 10^{8} m/s$), k_B is the Boltzmann constant ($1.3806 \times 10^{-23} J/K$), $B_{surface}$ is the blackbody spectral radiance in $W/m^2/\mu m/sr$ coming from the surface, and $I(\lambda)$ is the spectral radiance from the surface modified by emissivity (i.e. the surface signal). The signal measured by the hypothetical sensor at altitude was calculated using the radiative transfer equation:

$$I_\lambda(s) = \left[I_\lambda(0) \cdot exp\left[-\int_0^s k_\lambda(s')ds'\right]\right] + \int_0^s k_\lambda(s') \cdot B_\lambda(T(s')) \cdot exp\left[-\int_{s'}^s k_\lambda(s'')ds''\right] ds' \tag{2}$$

where $I_\lambda(s)$ is the spectral radiance reaching point s, $I_\lambda(0)$ is $I(\lambda)$ from eq. (1) for an altitude of 0 km, k_λ are the wavelength and altitude dependent volume absorption and emission coefficients of the atmosphere, and B_λ is the emission by the atmosphere. The first part of eq. (2) describes the signal transmitted through the atmosphere to point s; the second part (+ …) describes emission at any point, s', in the atmosphere and its subsequent absorption by the atmosphere as it travels to point s. Eq. (2) was discretized into a simple 1-D model below in eq. (3), in which Δs is set equal to 1 km.

$$I_\lambda(s) = \left[I_\lambda(0)\cdot exp\left[-\sum_{i=1}^{s} k_\lambda(i)\times\Delta s\right]\right] + \sum_{i=1}^{s} k_\lambda(i)\times\Delta s\times B_\lambda(T(s(i)))\cdot exp\left[-\sum_{j=i}^{s} k_\lambda(j)\times\Delta s\right] \quad (3)$$

We calculated the scattering footprint using a path integral approach described by Ashikhmin et al. (2004). In this work, the authors developed a simple analytical equation to estimate the blurring of light due to multiple scattering in spatially inhomogeneous scattering media. They begin with the most general case of light transport in arbitrary media, the time-dependent radiative transport equation. They then express this as a convolution of the initial source radiance distribution with a Green's function (AKA Green's propagator or evolution operator). They break the Green's function into 2 parts, an unscattered or single-scattered part and a multiply scattered part, and then solve these separately using the path integral approach. From this, they derive an analytical equation, eq. (4), with which to estimate spatial blur of a light ray (Ashikhmin et al., 2004). We refer the interested reader to their work, Ashikhmin et al. (2004), and contained references for more information.

$$w^2 = \left(\frac{1}{2}\right)\left(\frac{2a}{3S} + \frac{16\alpha}{bS^3}\right)^{-1} \quad (4)$$

Eq. (4) calculates the scattering footprint, in which w is the scattering footprint (referred to as spatial blur in Ashikhmin et al. (2004); spatial blur is defined as the width of the Gaussian distribution of paths around the most probable path perpendicular to the original direction of propagation), a the absorption coefficients, b the scattering coefficients, S the path length, and α is a function of the mean square scattering angle given by $1/(2\theta^2)$ (Ashikhmin et al., 2004). Eq. (4) assumes a collimated beam of light, that the medium is homogeneous, that deviation of paths from the most probable path are small enough to allow Taylor series expansion, and that the most probable path can be treated as a straight line without loss of generality (Ashikhmin et al., 2004). This method also assumes that the path taken by light scattered multiple times can be effectively mimicked by a Gaussian distribution. We used the Rayleigh scattering coefficients from the Lebonnois et al. (2015) total extinction coefficients as the scattering coefficients, b, and the remaining extinction coefficients as the absorption coefficients, a. The value of α is ultimately 0.013063. This comes from the equation for mean square scattering angle:

$$\theta^2 = 2\pi\int_0^\pi \theta^2 P(\theta) sin(\theta) d\theta \quad (5)$$

For Rayleigh scattering atmospheres, $P(\theta) = (3/4)(1 + cos^2\theta)$. We calculated the scattering footprint for each 1 km vertical section of the atmosphere and then summed these over the relevant altitudes for each model.

It is important to note that eq. (4) is not an exact answer; it provides a relatively simple formulation for estimating spatial blurring. In cases where more rigorous results were available (i.e., blurring estimates from a more accurate source), blurring estimates from eq. (4) were within a factor of 2 (Ashikhmin et al., 2004). This is important to keep in mind when interpreting the scattering footprints calculated here. This equation is also meant for a collimated beam of light. Emission from the surface of Venus is not as a set of parallel rays, but as rays with non-uniform directions. We assume that this method will then give the smallest possible scattering footprint and provide a constraint on possible footprint sizes.

We assumed thermodynamic equilibrium and therefore that Kirchoff's law applies (Hashimoto et al., 2008). This allowed the use of total extinction coefficients from Lebonnois et al. (2015) to be also used as total emission coefficients for the atmosphere. This data set is composed of 6 different opacities that combine to create the total extinction coefficients: 1) the gas opacities (e.g., CO_2, H_2O), 2) the vertical distribution of cloud particles, 3) collision-induced absorption for H_2O, 4) collision-induced absorption for CO_2, 5) opacity due to Rayleigh scattering by CO_2 and N_2, and 6) an added continuum to compensate for line-by-line approximations in the High Resolution Transmission (HITRAN) 2008 and High-Temperature Molecular Spectroscopic (HITEMP) 2010 databases (Lebonnois et al., 2015; Rothman et al., 2010). The total extinction coefficients extended in wavelength from 0.7 to 250 μm, in altitude from 0 to 100 km, and in presure from 92 to 2.6114 bars in unevenly spaced windows (Lebonnois et al., 2015). Wavelength window spacing varies from a maximum of 0.0141 μm to a minimum of 0.0014 μm, and a median of 0.0025 μm from 0.7 to 1.5 μm (these are the primary wavelengths of interest; the maximum and median change to 106.24 and 0.0059 μm if all wavelengths are considered). Altitude window thickness varies from as little as 0.02 km beneath 5 km altitude to as high as 3.91 km above 5 km with a median of 1.82 km. Pressure windows vary in thickness from as much as 8.45 bar to as little as 0.35 bar with a median of 3.57 bar. We interpolated the total extinction coefficients with respect to altitude to a 1 km spacing (Δs) using a piecewise cubic hermite interpolating polynomial (PCHIP) to reduce inaccuracies arising from the discretization of an integral. We also assumed a nadir viewing angle, plane-parallel and homogeneous slab layers, and a Lambertian surface that equally emits in all directions. The total extinction coefficients from Lebonnois et al. (2015) for the NIR range are only valid beneath the cloud deck. Lebonnois et al. (2015) used a simplified approximation of cloud scattering to calculate their total extinction coefficients. This approximation worked well at long wavelengths and reproduced observed top-of-atmosphere signals, but failed to reproduce observed top-of-atmosphere signals in the NIR (Lebonnois et al., 2015). For this reason, we considered our calculations valid only for altitudes of 50 km or below. Lastly, we assumed that Rayleigh scattering dominated beneath the cloud deck (Moroz, 2002). This is necessary for the use of eq. (4), which only considers the effects of Rayleigh scattering. The inclusion of the cloud deck would require us to account for Mie scattering and is a far more complicated issue. For these reasons, we treated 40 km as our nominal altitude. This altitude may be over-optimistic as particulate absorbers extend from the cloud deck down to altitudes as low as 30 km (Moroz, 2002) and possibly even as low as 10 km (Haus and Arnold, 2010), which would require calculations of Mie scattering for greater accuracy and precision, but we considered this acceptable for our purposes.

To the authors' knowledge, no formal criterion for an atmospheric window exists. It is often defined as a portion of the electromagnetic spectrum at which a signal transmits through the atmosphere with minimal distortion or absorption (e.g., Jensen, 2007; Lillesand et al., 2015). We used the arbitrary criterion that the spectral radiance from the target of interest, the surface in this case, must be equal to or greater than 50% of the signal that arrives at the sensor. As we are interested in the ability to view the surface, the spectral radiance of the surface must be greater than or equal to the cumulative spectral radiance of the atmosphere through which it passes. This likely excludes some bands from which surface information could be extracted, especially when considering that the effects of atmospheric distortion and absorption can be largely removed if data from multiple bands are considered (Haus and Arnold, 2010). This also excludes any effect that stacking may have in improving the signal to noise ratio and our ability to filter noise from extremely weak signals (e.g., Shalygin et al., 2015; Smrekar et al., 2010). However, we considered this an effective first order criterion by which to identify potentially useful surface viewing bands.

4. Results and discussion

4.1. Surface viewing atmospheric windows

Although our modeling extends from 0.7 to 250 μm, we only show wavelengths from 0.7 to 1.50 μm as the surface viewing atmospheric windows are all contained within this smaller range. Fig. 1a depicts the modeled spectral radiance reaching 10 and 40 km sensor altitudes for an assumed surface emissivity of 1, surface temperature of 735 K, and

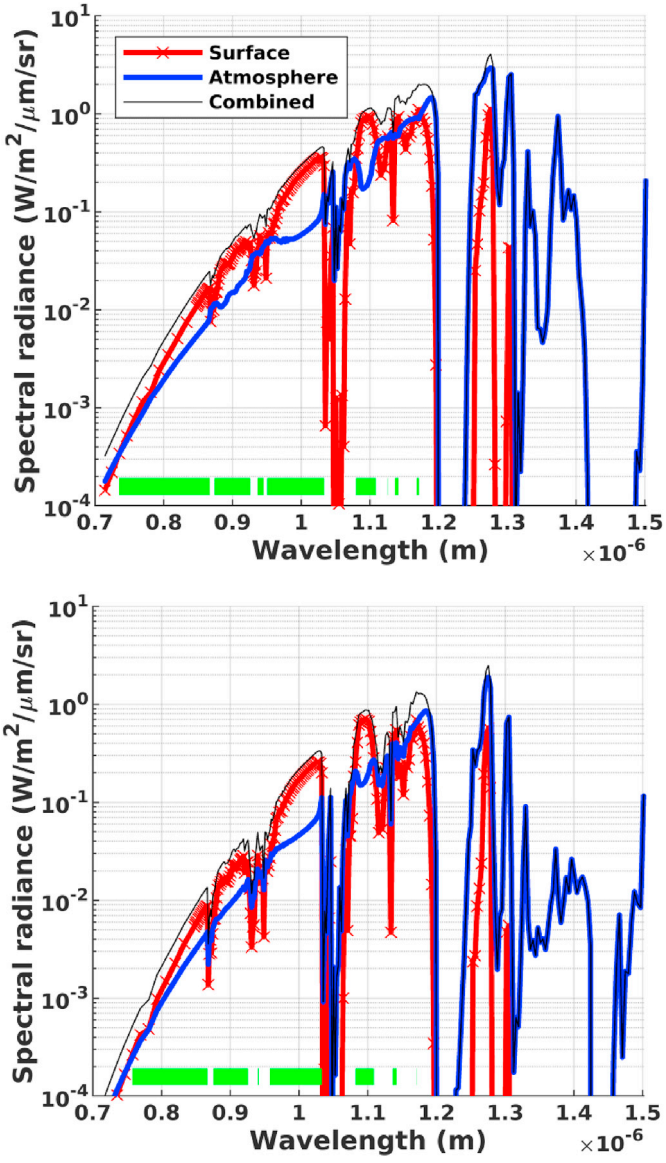

Fig. 1. a, Top: Modeled spectral radiance at 10 km altitude. b, Bottom: Modeled spectral radiance at 40 km altitude. Symbols are surface emission (red line with 'x's), the atmospheric emission (thick blue line), the combined signal (thin black line) assuming an emissivity of unity (1), and surface viewing atmospheric windows (green bar) for surface temperature of 735 K, and temperature profile of Seiff et al. (1985). Atmospheric windows are between 0.85 and 1.16 μm, similar to the already identified satellite atmospheric windows, but with expanded width. The surface signal decreases approximately 30% from 10 km to 40 km, but is largely the same, whereas the modeled atmospheric signal decreases significantly. (For interpretation of the references to color in this figure legend, the reader is referred to the Web version of this article.)

temperature profile of Seiff et al. (1985). After considering inaccuracies with the model above the cloud deck (e.g., the inaccurate cloud scattering and absorption), it is reasonably consistent with what is observed from space; multiplying our calculated total nightside radiances (combined surface and atmospheric emission) at 100 km by factors of 3–10, 1–2, 1.5–3, and 1/2–3/4 for the windows at 1.0, 1.10, 1.18, and 1.27 μm, respectively, puts them within the range of observed nightside radiances (Haus and Arnold, 2010). Qualitatively, the two plots of the surface signal in Fig. 1 are nearly identical. The effect of sensor altitude on identified bands is minor and limited primarily to the step from 10 km to 20 km altitude. The most notable change is the drop in the atmospheric signal at relatively long wavelengths (~1.3–1.5 μm) when the sensor height was varied from 10 to 40 km. The value of the surface, as well as atmospheric, signal at wavelengths >1.1 μm decreases significantly from 10 to 20 km due to the much stronger absorption and scattering by the denser atmosphere at low altitudes. At shorter wavelengths, the surface signal decreases by ~30% from 10 to 40 km. Overall, modeled surface emission decreases slightly (~30%) at shorter wavelengths (<1.1 μm) with increasing absorption at longer wavelengths. As defined above, surface viewing atmospheric windows only appear at wavelengths less than 1.2 μm. These are listed in Table 1 for altitudes of 10, 20, and 40 km. From 10 to 20 km, total bandwidth for which radiance from the surface exceeds or equals the atmospheric radiance decreases by 16.6% with effectively no further decrease at higher altitudes (the 0.938 μm wavelength is lost) and only the strength of the signal changes. This is qualitatively expected as the majority of the lower atmosphere (and hence the optically thickest portion of it) resides near the surface. Because of this, surface signal absorption and atmospheric emission are therefore greatest near the surface and decrease rapidly with altitude. From this, we interpret that changes in sensor altitude have a negligible effect on the surface viewing atmospheric windows. This apparent insensitivity to sensor altitude would allow a sensor to be deployed at any altitude convenient for the sensor system or mission requirements.

Fig. 2 depicts the effect of emissivity on the modeled spectral radiance reaching our nominal altitude of 40 km with surface temperature of 735 K and temperature profile of Seiff et al. (1985). Reducing emissivity reduces the modeled surface signal proportionally. The windows identified for emissivities of 1.0, 0.95, and 0.86 are largely the same, with some minor loss of available wavelengths for surface viewing below 0.86 μm as emissivity decreases. The lowest emissivity of 0.7 results in the fewest and narrowest set of atmospheric windows with a relative decrease in bandwidth of 32.3% from the 1.0 emissivity case. Surface viewing windows are listed in Table 2. At this lowest emissivity, we identified 4 atmospheric windows centered near 0.84, 0.90, 1.0, and 1.1 μm. These windows peak at approximately the same wavelengths as the five previously identified satellite windows (Allen and Crawford, 1984; Carlson et al., 1991; Crisp et al., 1991; Crisp and Titov, 1997; Peralta et al., 2017; Helbert et al., 2018), save for the 1.14–1.19 μm window which does not meet our criterion. The fifth, 1.14–1.19 μm, is excluded due to the stringency of the selected atmospheric window criterion and may be invalid due to inaccuracies in HITEMP 2010 (Arney et al., 2014), which are discussed further below. At the emissivity of the next lowest emissivity material, 0.86, part of the 1.14–1.19 window meets the 50% criterion and is identified as a surface viewing atmospheric window. As discussed below, a softer criterion would result in more of the long wavelength satellite window being identified as an atmospheric window, as well as result in windows that are broader in terms of wavelength. Surface signal decreased proportionally to emissivity due to the approximation of a constant emissivity. In reality, the emissivity of a material varies with wavelength as well as other conditions (e.g.,

Table 1
Surface viewing atmospheric windows with height. Surface temperature and atmospheric temperature with height are the surface average of 735 K and that of Seiff et al. (1985). Emissivity is set to unity (1). The atmospheric windows identified beneath the cloud deck are all wider save for the 1.14–1.19 μm window, which is almost completely excluded.

Height (km)	Surface Viewing Atmospheric Windows (μm)
10	0.735–0.867; 0.871; 0.874–0.926; 0.936–0.946; 0.951–1.033; 1.080–1.109; 1.126; 1.136–1.142[a]; 1.168–1.171[a]
20	0.758–0.867; 0.876–0.926; 0.938–0.942; 0.952; 0.958–1.033; 1.082–1.109; 1.136–1.142[a]; 1.171[a]
40	0.758–0.867; 0.876–0.926; 0.940–0.942; 0.952; 0.958–1.033; 1.082–1.109; 1.136–1.142[a]; 1.171[a]

[a] CO_2 opacity from approximately 1.10–1.18 μm is under-predicted by HITEMP 2010 and requires more accurate modeling to constrain their potential usefulness (Arney et al., 2014).

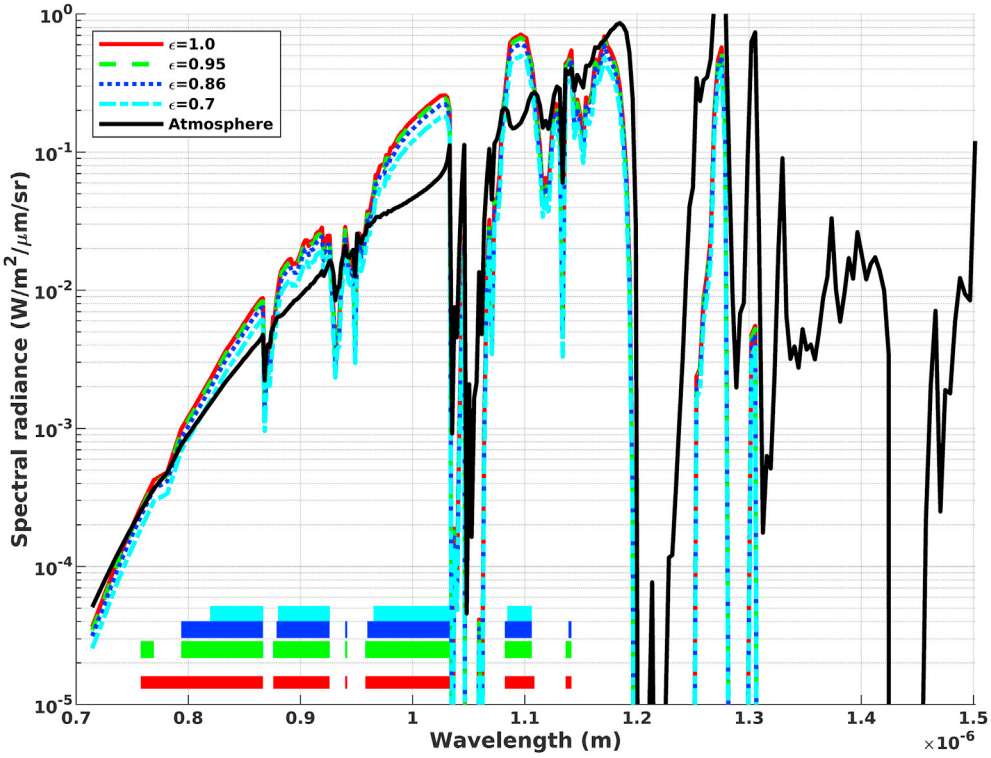

Fig. 2. Modeled spectral radiance at 40 km altitude for materials of differing emissivity. Colored bars near the x-axis indicate identified surface viewing atmospheric windows with matching colors. Surface temperature and atmospheric profile are 735 K and the profile from Seiff et al. (1985). The surface signals are morphologically identical as the emissivity variation used here is a constant and not wavelength dependent. Atmospheric windows are robust to large emissivity variations below ~1.14 μm, though the change in emissivity does cause a significant weakening of the surface signal. The band from 1.14 to 1.19 μm, a satellite atmospheric window, is the most susceptible to changes in emissivity as shown by its decrease near to or beneath the atmospheric emission signal. (For interpretation of the references to color in this figure legend, the reader is referred to the Web version of this article.)

Table 2
Surface viewing atmospheric windows by emissivity. Surface temperature and atmospheric temperature with height are the surface average of 735 K and that of Seiff et al. (1985). Sensor height is kept constant at 40 km. The low emissivity case had the greatest constraints on atmospheric windows with only 4 identified. At this low emissivity, the satellite window from 1.14 to 1.19 μm is absent.

Emissivity	Surface Viewing Atmospheric Windows (μm)
1.0	0.758–0.867; 0.876–0.926; 0.940–0.942; 0.952; 0.958–1.033; 1.082–1.109; 1.136–1.142[a]; 1.171[a]
0.95	0.758–0.769; 0.794–0.867; 0.876–0.926; 0.940–0.942; 0.952; 0.958–1.033; 1.082–1.106; 1.136–1.142[a]; 1.171[a]
0.86	0.794–0.867; 0.876; 0.879–0.926; 0.940–0.942; 0.960–1.033; 1.082–1.106; 1.139–1.142[a]
0.7	0.820–0.867; 0.880–0.926; 0.965–1.033; 1.085–1.106

[a] CO_2 opacity from approximately 1.10–1.18 μm is under-predicted by HITEMP 2010 and requires more accurate modeling to constrain their potential usefulness (Arney et al., 2014).

Gilmore et al., 2015; Jensen, 2007; Lillesand et al., 2015; Hashimoto et al., 2008). Although the emissivity varies with wavelength, the bulk emissivities we used here broadly match those of the emissivities measured in a laboratory setting. The DLR is currently obtaining emissivity data for numerous rocks at the temperatures of Venus and at the wavelengths that correspond to the satellite atmospheric windows (Helbert et al., 2018). Ostensibly, this expanded data will allow for more accurate forward modeling and inversion of the surface signal for various rock types and characteristics in the future. Smrekar et al. (2010) examined Visible and Infrared Thermal Imaging Spectrometer (VIRTIS) emissivity data on and around Idunn Mons. They posited that if the high emissivity anomalies of this region are relatively unweathered basalt with an emissivity of 0.85–0.9, then the detected 12% decrease in flux implies a weathered background emissivity as low as 0.5 to 0.6, most consistent with fine-grained hematite (Smrekar et al., 2010). At an emissivity as low as 0.5 for an average surface temperature and profile and a sensor altitude of 40 km, the identified surface viewing atmospheric windows are similar to, though smaller than, the 0.7 emissivity case. These shrink to 0.883–0.891, 0.901–0.919, 0.967–1.031, and 1.085–1.104 μm. This indicates that, even at significantly reduced emissivity, there are numerous bands with which it is possible to view and constrain the possible composition and characteristics of the surface.

Fig. 3 displays the effect of surface elevation (and therefore surface temperature and pressure) variation on the modeled spectral radiance

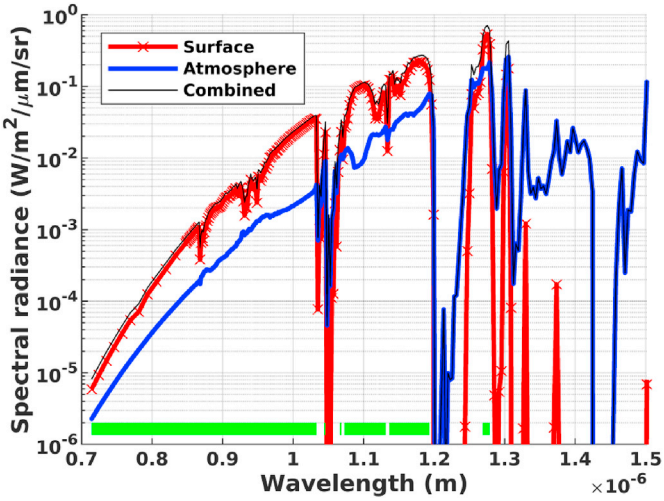

Fig. 3. Left: modeled spectral radiance from surface at 11 km above MPR to 40 km sensor altitude. Surface emission is the red line with 'x's, the atmospheric emission the thick blue line, and the combined signal the thin black line assuming an emissivity of unity (1). The elevated surface reduces surface temperature to 650.6 K. As compared to Fig. 1b, the emitted signal is weaker at wavelengths <1.2 μm and stronger at ~1.27 μm. The atmospheric signal is much weaker, causing an expansion of the modeled atmospheric windows. The ~1.27 μm wavelength is normally blocked by O2 airglow at ~95 km (Peralta et al., 2017), but should be valid beneath that altitude. (For interpretation of the references to color in this figure legend, the reader is referred to the Web version of this article.)

Table 3
Surface viewing atmospheric windows of an elevated surface source. Surface elevation has been increased to 11 km above MPR, resulting in a surface temperature of 650.6 K. The temperature profile from Seiff et al. (1985) is used. Sensor altitude is kept constant at 40 km.

Emissivity	Surface Viewing Atmospheric Windows (μm)
1.0	0.714–1.033; 1.044–1.046; 1.066–1.068; 1.073–1.131[b]; 1.136–1.193[b]; 1.269–1.279[a]
0.95	0.714–1.033; 1.044–1.046; 1.066–1.068; 1.073–1.131[b]; 1.136–1.193[b]; 1.269–1.279[a]
0.86	0.714–1.033; 1.044–1.046; 1.066–1.068; 1.073–1.131[b]; 1.136–1.193[b]; 1.269–1.279[a]
0.7	0.714–1.033; 1.046; 1.068; 1.073–1.114; 1.124–1.131[b]; 1.136–1.191[b]; 1.269–1.279

[a] This window is invalid above the cloud deck as a surface viewing atmospheric window due to airglow at ~95 km overpowering all surface signal at these wavelengths (Peralta et al., 2017) and the approximations of Lebonnois et al. (2015). Beneath the cloud deck, this window should be valid.

[b] CO_2 opacity from approximately 1.10–1.18 μm is under-predicted by HITEMP 2010 and requires more accurate modeling to constrain their potential usefulness (Arney et al., 2014).

reaching our nominal altitude of 40 km. We set the surface elevation to 11 km and used the temperature provided by Seiff et al. (1985) at 11 km in order to simulate conditions as might be seen at the highest location of Ishtar Terra, near Maxwell Montes, with a corresponding surface temperature of 650 K (Haus and Arnold, 2010). This reduced the surface pressure to 39.17% of its original value, 36 bars. Table 3 lists the identified atmospheric windows. Bandwidth relative to the nominal elevation case increased by 40.9% and a new band became available centered near 1.27 μm. Identified windows range almost continuously from 0.714 μm to 1.193 μm even at the lowest emissivity of 0.7. The 85 K decrease in temperature reduces the total signal from the surface. However, the increased altitude also excludes a portion of the lower atmosphere which would otherwise have higher temperature, pressure, absorber mass, and extinction coefficients, meaning the absorption and emission by the atmosphere are reduced again not only because of the reduced temperature, but also because of the reduced absorber mass and reduced collision-induced absorption. The combined effect is a total decrease in signal and a relative increase in the ratio of the surface to atmosphere signal. This agrees with the results of Moroz (2002), which show an increase in the visibility factor for an elevated surface position of 6 km compared to the nominal surface elevation of 0 km. We identified an additional window at ~1.27 μm that is obscured by atmospheric emission under other conditions; O_2 airglow at ~95 km overpowers the surface signal at higher altitudes on the nightside, preventing its use by satellites for studying the surface (Peralta et al., 2017). This added window should be valid beneath the cloud deck. These combine to make regions of elevated terrain prime targets for any spectroscopic study to determine composition as the deleterious effects of the atmosphere on the desired signal are reduced and the available wavelengths to study the surface are greatly increased.

Fig. 4 depicts the effect of the variation of the temperature profile on the modeled spectral radiance as might exist between different regions (Haus and Arnold, 2010). We set the source elevation to 0 km, sensor altitude to 40 km, and emissivity to unity (1). The surface temperature and profile of Seiff et al. (1985) were modeled with 20 K added and subtracted to explore the temperature variation as observed among the multiple atmospheric probes that have descended through the Venusian atmosphere and surface (Crisp and Titov, 1997). Identified windows are listed in Table 4. Quantitatively, modeled signal strength increases with increased temperature and decreases with decreased temperature, most clearly visible at shorter wavelengths. Decreased temperature results in minor improvement in total bandwidth available compared to the case of increased temperature by 13.8%. This is most readily explained by a greater sensitivity to changes in temperature of the atmosphere at low altitudes which cause larger changes in emission as compared to the surface. Qualitatively, the temperature variation has little effect on the relative strengths of the surface signal as compared to the atmospheric

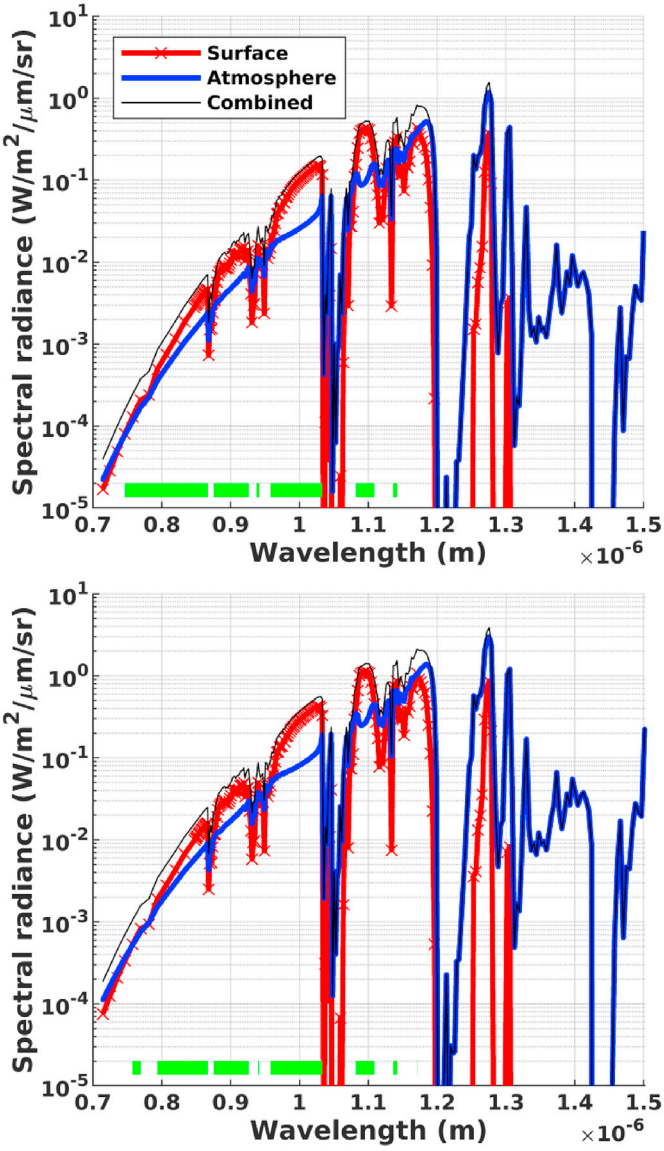

Fig. 4. Modeled spectral radiance from surface with minor temperature variation. Top: minus 20 K; bottom: plus 20 K. Emissivity is set to unity (1). The temperature has been modified plus and minus 20 K. The signal strength is minorly altered by the 40 K difference between the two models with the warming case having slightly more restricted surface-viewing windows, but is otherwise qualitatively similar with near identical atmospheric windows.

Table 4
Surface viewing atmospheric windows for minor temperature variation. Surface temperature and atmospheric temperature with height are the surface average of 735 K and that of Seiff et al. (1985) plus and minus 20 K. Emissivity is set to unity (1). The resulting atmospheric windows are nearly identical to each other.

ΔT	Surface Viewing Atmospheric Windows (μm)
+20 K	0.758–0.769; 0.794–0.867; 0.876–0.926; 0.940–0.942; 0.952; 0.958–1.033; 1.082–1.109; 1.136–1.142[a]; 1.171[a]
−20 K	0.746–0.867; 0.871; 0.876–0.926; 0.938–0.942; 0.952; 0.958–1.033; 1.082–1.109; 1.136–1.142[a]; 1.171[a]

[a] CO_2 opacity from approximately 1.10–1.18 μm is under-predicted by HITEMP 2010 and requires more accurate modeling to constrain their potential usefulness (Arney et al., 2014).

emission. Table 4 shows that the two models have largely similar atmospheric windows. Some of the windows of the increased temperature model are slightly narrower as compared to the case of decreased temperature. Blocked wavelengths in the windows near 0.75 and 0.78 μm for the elevated temperature model are the most notable differences from the reduced temperature model. Overall, this indicates that changes in regional temperature do not affect or have only a minor effect on surface viewing atmospheric windows.

Generally, the strongest signal and broadest window occur at 1.1 μm. Throughout all of the parameters explored, the 1.1 μm window retained a high signal output and broad bandwidth. This, combined with the relatively low contribution from the atmosphere, indicates the 1.1 μm window is the most important for obtaining data about the surface. For our nominal conditions, this is followed by the 1.0 μm window. The 1.14 μm window often has a higher peak signal strength than the 1.0 μm window, but is narrow comparatively and has a lower cumulative signal output. This makes the 1.0 and 1.1 μm windows the most important as most of Venus falls near our nominal conditions. In the case of an elevated location, this changes drastically. The 1.14–1.19 and 1.27 μm windows increase significantly in strength over the 1.0 μm window. The 1.1 μm window retains a relatively high and broad signal output, though of lower signal than the 1.14–1.19 and 1.27 μm windows. These three (1.1, 1.14–1.19, and 1.27 μm) become the most important for elevated surfaces. Any mission that exploits the improved visibility beneath the cloud decks should make use of 0.7–1.0, 1.1, and 1.27 μm windows as these provide a comprehensive ability to extract information about the surface at the various possible surface elevations. Compared to the already identified satellite atmospheric windows, the potential surface viewing atmospheric windows beneath the cloud deck as identified here are significantly wider and of much greater strength. Comparing actual satellite measurements to the modeled data for 40 km altitude indicates an order of magnitude increase in the total signal. This much stronger signal reduces the need for averaging multiple images of the surface as has been needed to use VIRTIS emissivity data (e.g., Shalygin et al., 2015; Smrekar et al., 2010; Kappel et al., 2016), though this would come at the cost of reduced field of view as compared to a sensor at satellite altitude. The longest wavelength identified as a potential surface viewing atmospheric window is 1.27 μm, which is still well within the near-infrared. At this wavelength, airglow caused by the recombination of oxygen atoms at ~95 km overpowers any surface signal that might be observed by a satellite (Peralta et al., 2017), but would be valid for any system beneath the cloud deck. Not all of the previously known satellite windows are identified as potential surface viewing atmospheric windows. The window from 1.14 to 1.19 μm is often absent, only appearing as a window in its entirety when the surface is elevated to 11 km. For the nominal conditions, the closest to this missing window is a pair of windows within that range at 1.136–1.142 and 1.171 μm. This absence is a result of the stringent atmospheric window condition which requires that 50% or more of the signal measured at the hypothetical sensor comes from the surface. For much of the satellite window from 1.14 to 1.19 μm, the surface signal is a large portion of the modeled total signal, but less than 50%. A more relaxed requirement, such as 25% surface signal, could include more of the 1.14–1.19 μm window as well as other wavelengths, making nearly all of the NIR spectrum useful for viewing the surface. As an example, the atmospheric windows for $\varepsilon = 0.95$ with a sensor at 40 km altitude and criterion of 25% expand to 0.714–0.947, 0.951–1.033, 1.073–1.114, 1.119–1.131, and 1.136–1.182 μm. The dominance of atmospheric emission precludes the immediate quantitative use of data from the wavelengths longer than 1.17 μm in our nominal conditions. However, provided data at multiple wavelengths, the deleterious effects of atmospheric absorption and emission can be mitigated to obtain data that primarily carries information about the surface through radiometric calibration (Haus and Arnold, 2010; Jensen, 2007).

Our analysis has been limited to the nightside of Venus as scattered sunlight overwhelms surface emissions on the dayside. In reality, limiting an aerial mission to only the nightside of the planet is unrealistic and raises the questions: Can we extract surface information from the dayside? What would be required in order to view the surface on the dayside of Venus? We posit this is conceptually possible, though most likely impossible with our current knowledge of Venus and logistical capabilities. Even at the low altitude of 10 km, downward solar radiance as measured by the Venera 13 descent probe exceeds thermal emission from the surface by a factor of 10–100 at the relevant wavelengths and becomes progressively worse at higher altitudes (Moroz et al., 1985; Moroz, 2002; Titov et al., 2007). At the surface, this drops to a factor of approximately 5–10 (Moroz et al., 1985; Moroz, 2002; Titov et al., 2007). This energy would then be mostly absorped and then partly reflected. For a basaltic material ($\varepsilon \approx 0.9$), a downward radiance of 10 $W/m^2/\mu m/sr$ (the approximate downwelling at the surface at 1.0 μm) would result in a reflection of ~1 $W/m^2/\mu m/sr$; for felsic ($\varepsilon \approx 0.7$), ~3 $W/m^2/\mu m/sr$. This would make the emission smaller than the reflection by only a few factors at most near the surface. At our nominal altitude, the reflected components are ~0.5 and ~1.5 $W/m^2/\mu m/sr$ for mafic and felsic materials, respectively. Adding the emitted component increases the total surface signal to ~0.7 and ~1.6 $W/m^2/\mu m/sr$. Though both the emission and reflection are small, this simple analysis suggests these small signals could be detected and differentiated to identify felsic versus mafic terrain if the signal error is small. We believe the more difficult step would be the requisite cloud corrections. As solar radiation passes through the clouds, the cloud deck absorbs differently at each wavelength depending on the spatially and temporally varying properties of the clouds. Removing the effect of this non-linearly modified sunlight requires precise knowledge of the cloud and atmosphere properties at the time of measurement acquisition and for the particular ground projected area of each pixel as well as very low uncertainty (i.e., high precision and accuracy). Corrections for clouds have been successfully performed on Earth using hyperspectral data (e.g., Schlapfer et al., 2009). Bands sensitive to particular phenomenon and atmospheric heights provide information that can be used to calculate absorption, scattering, and emission by the different parts of the atmosphere. Hypothetically, an aerial platform somehow viewing in all directions around it or an accompanying orbital platform could collect this requisite hyperspectral correction data. However, the terrestrial examples have typically been thin clouds many orders of magnitude smaller in terms of their optical depths relative to the Venusian clouds, and this correction has only been done for observations made above the clouds of Earth. Kappel et al. (2016) performed error analysis related to surface emissivity retrieval from VIRTIS/VEX measurements from the nightside using 3 wavelengths: 1.02, 1.10, and 1.18 μm. Using these bands, they estimated true emissivity retrieval errors of 3–10% related to temporally varying atmospheric parameters and 9–16% related to spatially varying atmospheric parameters (Kappel et al., 2016). At these wavelengths, a true emissivity retrieval error of as little as 6% would cause a measurement to overlap the laboratory measured emissivities of both felsic and mafic materials (Helbert et al., 2018). If we assume an upwelling scattered solar radiation component of ~10 $W/m^2/\mu m/sr$at our nominal altitude of 40 km and at 1.0 μm, an atmospheric correction error of 5%, resulting in an absolute error of ~0.5 $W/m^2/\mu m/sr$, is enough to make the dayside surface signals from a mafic and felsic material indistinguishable. This combines to make useful dayside observations of the surface possible, though logistically very difficult as a very accurate and precise characterization of the atmosphere and its effect on incoming sunlight at the time of measurement is required.

4.2. Scattering footprint

To study the scattering footprint, we explored the effect of varying the sensor altitude and surface elevation using an equation derived in Ashikhmin et al. (2004). Figs. 5 and 6 display the scattering footprint for various model conditions. Fig. 5 shows the effect of wavelength and various sensor altitudes on the scattering footprint. Shorter wavelengths

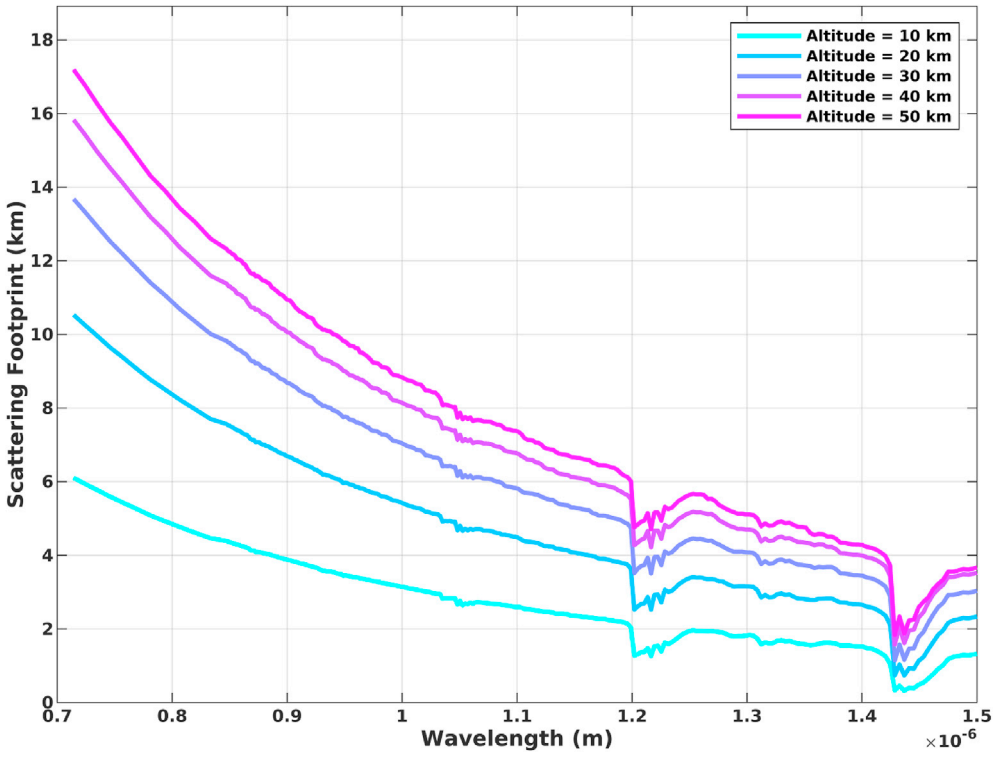

Fig. 5. Wavelength vs scattering footprint for multiple sensor altitudes. The scattering effect of the atmosphere decreases with increasing wavelength. The increase in footprint size exponentially decreases with sensor altitude. The step functions in scattering footprint at ~1.2 and 1.42 μm are caused by spikes in the CO2 absorption coefficients at these wavelengths. These correlate with large drops in signal shown in the plots of Fig. 1 through 4.

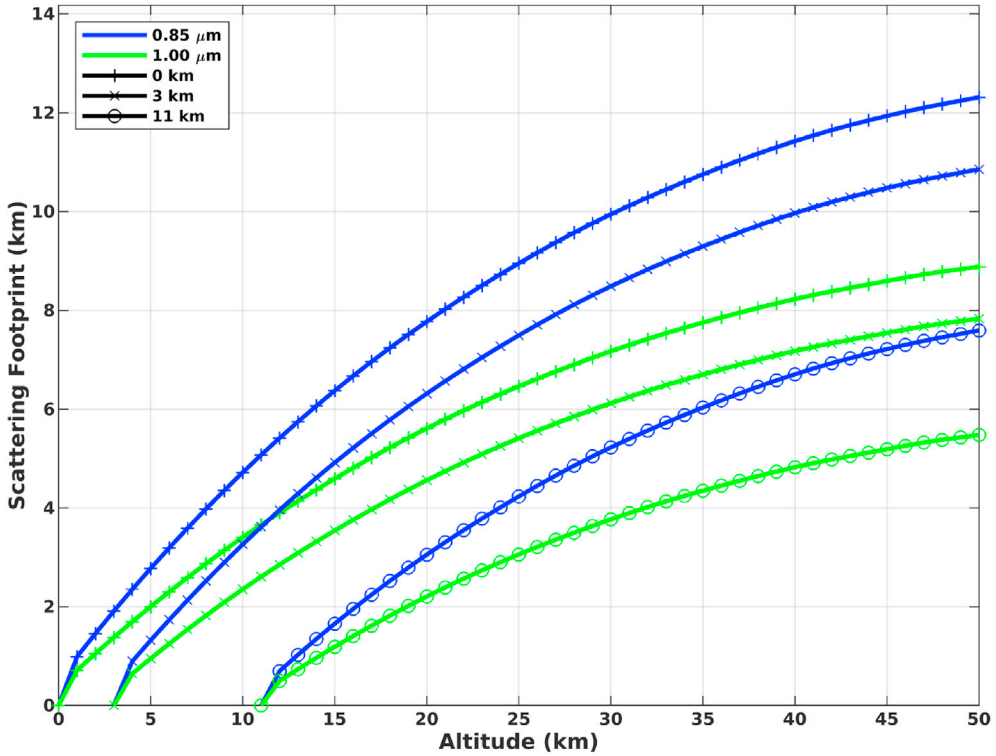

Fig. 6. Sensor altitude vs scattering footprint for multiple surface elevations. Increasing surface elevation significantly improves the scattering footprint, similar to the atmospheric window expansion for elevated regions. The scattering footprint for system altitudes of 40–50 km equals or exceeds 5 km, making the Magellan GTDR sufficient to remove the effect of surface elevation from the observed emissivity.

experience greater amounts of scattering. This is expected as Rayleigh scattering is highly wavelength dependent; smaller wavelengths scatter more effectively than longer wavelengths. The increase in footprint size with sensor altitude decreases as the sensor is modeled at progressively higher altitudes. At the shortest wavelength, an increase in altitude from the surface to 10 km increases the scattering footprint by ≈~6 km, whereas a shift from an altitude of 40–50 km increases the footprint by only ~1.5 km. This results from the greater density, temperature, and absorption and scattering coefficients in the lowest portion of the atmosphere. At our nominal altitude of 40 km, the 0.85 μm window has a footprint of ~11 km, the 1.0 μm a footprint of ~8 km, and the 1.1 μm a footprint of ~7 km. This is approximately an order of magnitude improvement over the 50–100 km footprint estimated for orbital systems (Moroz, 2002; Hashimoto and Imamura, 2001). In Fig. 5, a step function occurs at ~1.2 and 1.42 μm at which the scattering footprint decreases significantly. This would suggest that these wavelengths may be useful for viewing the surface as these have the smallest scattering footprint. However, these wavelengths are useless for studying the surface as these have negligible surface or atmospheric signal. Significant spikes in CO_2 absorption/emission occur at these wavelengths and cause the surface and atmospheric signal to drastically decrease. This spike in absorption causes a decrease in the calculated scattering footprint due to the inverse dependence on absorption. Fig. 6 elucidates the effect of surface elevation at 0, 3, and 11 km on the scattering footprint for wavelengths of 0.85 and 1.0 μm. The longer wavelength is less affected by scattering. Increased surface elevation improves the scattering footprint by placing the signal source above the densest (and most scattering) part of the atmosphere, similar to the diminished change in scattering footprint with increased sensor altitude, as well as by reducing the distance between the target source and the sensor. The footprint calculated for the 0.85 μm wavelength decreases from ~11.5 km to ~10 km and then to ~6.5 km for our nominal sensor altitude of 40 km as the surface elevation changes from 0 to 3 and then 11 km. At a wavelength of 1.0 μm, the scattering footprint reaches a value of ~4.8 km for a sensor altitude of 40 km and surface elevation of 11 km.

Overall, this makes the scattering footprint beneath the cloud deck approximately an order of magnitude better than that above the cloud deck (Moroz, 2002; Hashimoto and Imamura, 2001). This would reduce the effect of pixel mixing (the convolution of the signal from multiple sources overlapping each other) and better localize source targets. The smallest scattering footprint for our nominal conditions is ~5 km at a wavelength of 1.27 μm. This is approximately the same size as the Magellan Gridded Topographic Data Record (GTDR), which should allow the removal of surface elevation effects from emissivity measurements to obtain true emissivity. The size of the scattering footprint can be used as a proxy for the largest instantaneous field of view a pixel in a spectrometer system could have without loosing information. If we assume a scattering footprint of 10 km for our nominal altitude of 40 km, this makes the largest field of view allowable 0.25 radians. This is 3 orders of magnitude larger than the field of view on the VIRTIS instrument. Even if our calculated scattering footprint is off by several factors resulting in a true footprint of ~1 km, the field of view is 2 orders of magnitude larger (0.025 radians). This indicates that a spectrometer with a relatively poor field of view could still extract useful data without a loss of information. However, this does not address the specific needs of a VIRTIS-like for in-situ operation, such as the temperature requirements, which may not be feasible even within the relatively cool portions of the Venus atmosphere (Williams, 2019).

4.3. Possible uses

A complete inventory of every possible use of data acquired by a hypothetical spectrometer mission beneath the cloud deck is beyond this work. However, there are several possible uses worth discussing: 1) determination of broad rock types (e.g., felsic vs. mafic material); 2) location of recently actively lava flows and currently active volcanism; and 3) determination of the surface weathering oxidation state. 1) The DLR is pioneering the development of emissivity data at high temperatures of a variety of rocks and mineral assemblages (e.g., Helbert et al., 2018). The rocks to date have been relatively common igneous rocks, including basalt, trachybasalt, basaltic andesite, multiple rhyolites, granite, and anorthosite. These materials are difficult to distinguish with an emissivity measurement of a single wavelength, but are easily distinguished when multiple wavelengths are considered (Baines et al., 2000; Helbert et al., 2018). The potential expanded windows identified here could provide new constraints (data points) to help deconvolve the effect of other variables (e.g., grain size, surface roughness, etc. (Gilmore et al., 2015; Jensen, 2007; Hashimoto et al., 2008)) and ascertain definitive rock types for the surface of Venus (Helbert et al., 2018) and potentially answer if plate tectonics ever occurred in this planet's past. 2) The satellite atmospheric windows of Venus have already been used to search for recently and currently active volcanism on the surface of Venus (e.g., Smrekar et al., 2010; Shalygin et al., 2015; D'Incecco et al., 2017). Smrekar et al. (2010) examined emissivity values on and near the volcano Idunn Mons. By combining 1.5 years of VIRTIS imagery, the authors were able to locate regions of anomalously high emissivity. Assuming the surface is primarily basaltic, regions of low emissivity are weathered and those of high emissivity are unweathered, and these give ages of 2.5 million to 250 thousand years for lava flows coming from Idunn Mons. The work of D'Incecco et al. (2017) built on this by obtaining the best fit of created hypothetical emissivity maps, showing that the anomalous emissivity matched observed stratigraphic relationships (i.e., units higher in the stratigraphy have higher emissivity and are assumed therefore to be less weathered and younger). Shalygin et al. (2015) used relative changes in brightness at 1.01 μm in normalized Venus Monitoring Camera (VMC) imagery to identify persistent locations of elevated emission near Ganiki Chasma (a rift-like zone). These have been interpreted as changes in surface temperature due to the eruption of lavas (Shalygin et al., 2015). An aerial system at a low altitude with more available wavelengths would make the identification of active volcanism more robust thanks to improved signal-to-noise ratio, smaller instantaneous field of view, and a smaller scattering footprint that could better localize the source and reduce pixel mixing. 3) The surface oxidation state (AKA redox state) has the unique potential use of identifying the past water inventory of Venus (Pieters et al., 1986). Any past surface water of Venus has dissociated into hydrogen, which is lost to space, and into oxygen, which remains in the atmosphere until it reacts with a surface material to oxidize it. This process increases the proportion of Fe^{3+} atoms and causes the emissivity of the surface material to fall (Dyar et al., 2017). From this drop in emissivity, an estimate of past surface water can be derived. However, this requires a robust determination of the material imaged before a determination of redox state can be made (Dyar et al., 2017).

4.4. Caveats

We must mention several words of caution concerning the contents of this study and their validity. First, the results of this study are only valid for the nightside of Venus. The effect of scattering and absorption of sunlight has been ignored. On the dayside of Venus, these windows are entirely overridden by scattered sunlight (Peralta et al., 2017; Moroz, 2002; Kappel et al., 2016). Next, we wrote our own relatively simply radiative transfer model that has not been validated via comparison to other vetted modeling codes such as KARINE (Eymet, 2008). We excluded the possible effect of multiple scattering along boundary layers within the atmosphere. This is colloquially known as ghosting in seismic studies and has the potential to muddle any surface signal with spurious returns (Moroz, 2002; Hashimoto et al., 2008; Mueller et al., 2008; Kappel et al., 2016). This also excludes any possible effect from an undercloud haze (Moroz, 2002; Mueller et al., 2008; Haus and Arnold, 2010). This undercloud haze has the potential to drastically increase atmospheric absorption and therefore also emission, though it appears to

be temporally and regionally variable (Moroz, 2002; Haus and Arnold, 2010). Analysis of VIRTIS and VEX measurements suggests the effects of the undercloud haze may be completely mitigated by mesoscale downwellings in some cases (McGouldrick et al., 2012).

An aerial system beneath the cloud deck has the potential to provide significant improvement to our understanding of the emissivity of the surface of Venus, but is largely limited by a need for better calibration and ancillary data. The total extinction coefficients, in part, are extrapolated and theoretical values (Lebonnois et al., 2015). Any windows found between the wavelengths of 1.10 and 1.18 μm may not be valid as HITEMP 2010, which is the CO_2 line strength source for the total extinction coefficients used here, is known to underpredict the line strengths of CO_2 from 1.10 to 1.18 μm (Arney et al., 2014). This makes it entirely possible that any surface viewing window identified in or near this region of the electromagnetic spectrum may not exist and introduces some level of uncertainty. To remedy this will require a more accurate knowledge of CO_2 absorption/emission characteristics at these extreme temperature and pressure conditions. True emissivity is easily distorted by errors in temperature and topographic data, as well as by the models used to calibrate the emissivities (Smrekar et al., 2010; Shalygin et al., 2015; D'Incecco et al., 2017). Current topographic data is limited to altimetry data, with a 10–20 km footprint gridded to an ~5 km pixel size (Ford et al., 1993), or stereo-derived digital elevation models with a 1–2 km footprint that only cover 20% of Venus (Herrick et al., 2012). These topographic data are sufficient to remove the effect of varying surface elevation and therefore surface temperature for emissivity data collected from orbit as well as for our nominal case, though improved topographic data would reduce the error associated with the true emissivities inverted.

Finally, the equation we used to estimate scattering footprint is an idealization. It makes numerous assumptions and simplifications that negatively affect its accuracy. The results are within a factor of 2 when compared to rigorous test cases (Ashikhmin et al., 2004). This means the scattering footprint may be twice as large as that calculated here. Conversely, this could mean the scattering footprint is as little as half the values shown here. This equation was derived specifically for collimated light (Ashikhmin et al., 2004). The surface of Venus will not produce parallel light rays, but rather a diffuse set of rays which are scattered into random directions by the atmosphere. This makes the estimates derived from this equation the smallest possible footprints.

5. Conclusions

This work sought to find potential surface viewing atmospheric windows for surface emissions beneath the cloud deck of Venus that might be exploited by future missions in the range from 0.7 to 250 μm. For our nominal conditions, the atmospheric windows identified are essentially expanded versions of the previously identified atmospheric windows at 0.85, 0.9, 1.01, and 1.10 μm. The stringent conditions used here shrank the fifth satellite atmospheric window from 1.14 to 1.19 μm to two narrow atmospheric windows centered at 1.14 and 1.17 μm. Aside from the latter satellite band, all of these have significantly increased bandwidth. Emissivity of the surface material and surface elevation strongly affect which wavelengths we identified as atmospheric windows. Lower emissivities shrink the identified surface viewing atmospheric windows, and higher surface elevations expand the atmospheric windows and increases the overall surface-to-atmosphere signal ratio at the cost of reduced signal strength. Any mission that exploits the improved visibility beneath the cloud decks should make use of 0.7–1.0, 1.1, and 1.27 μm windows as these provide a comprehensive ability to extract information about the surface. The wavelengths from 1.14 to 1.19 may be useful, but require more accurate modeling to better constrain their potential usefulness as the HITEMP 2010 linelists under-predict CO_2 opacity at these spectra (Arney et al., 2014). Combined with future laboratory data being developed at the DLR and elsewhere, these atmospheric windows have the potential to elucidate the composition and redox state of the surface of Venus and answer questions about the tectonic and hydrologic history of the planet (Pieters et al., 1986; Hashimoto et al., 2008; Dyar et al., 2017; Helbert et al., 2017 & 2018).

Declaration of competing interest

None.

Acknowledgments

Comments from and discussions with G. Arney, S. Lebonnois, F. Meyer, and L. Glaze, improved this manuscript. We also thank the 2 anonymous reviewers for their commentary, which greatly improved this work. Partial funding for this work was provided by the Alaska Space Grant Program fund G10074 and Planetary Geology and Geophysics Program grant NNX14AM84G to R. Herrick.

References

Allen, D.A., Crawford, J.W., 1984. Cloud structure on the dark side of Venus. Nature 307. https://doi.org/10.1038/307222a0.

Arney, G., Meadows, V., Crisp, D., Schmidt, S.J., Bailey, J., Robinson, T., 2014. Spatially resolved measurements of H_2O, HCl, CO, OCS, SO_2, cloud opacity, and acid concentration in the Venus near-infrared spectral windows. J. Geophys. Res. Planets 119. https://doi.org/10.1002/2014JE004662.

Ashikhmin, M., Premoze, S., Ramamoorthi, R., Nayar, S., 2004. Blurring of light due to multiple scattering by participating medium: a path integral approach. Dept. Comput. Sci., Columbia Univ. https://doi.org/10.7916/D8CN7BRN. Technical Report CUCS-017-04.

Baines, K.H., Bellucci, G., Bibring, J.-P., Brown, R.H., Buratti, B.J., Bussoletti, E., Capaccioni, F., Cerroni, P., Clark, R.N., Coradini, A., Cruikshank, D.P., Drossart, P., Formisano, V., Jaumann, R., Langevin, Y., Matson, D.L., McCord, T.B., Mennella, V., Nelson, R.M., Nicholson, P.D., Sicardy, B., Sotin, C., Hansen, G.B., Aiello, J.J., Amici, S., 2000. Detection of sub-micron radiation from the surface of Venus by cassini/VIMS. Icarus 148. https://doi.org/10.1006/icar.2000.6519.

Bezard, B., de Bergh, C., 2007. Composition of the atmosphere of Venus below the clouds. J. Geophys. Res. 112 https://doi.org/10.1029/2006JE002794.

Carlson, R.W., Baines, K.H., Encrenaz, Th, Taylor, F.W., Drossart, P., Kamp, L.W., Pollack, J.B., Lellouch, E., Collard, A.D., Calcutt, S.B., Grinspoon, D., Weissman, P.R., Smythe, W.D., Ocampo, A.C., Danielson, G.E., Fanale, F.P., Johnson, T.V., Kieffer, H.H., Matson, D.L., McCord, T.B., Soderblom, L.A., 1991. Galileo infrared imaging spectroscopy measurements at Venus. Science 253, 1541–1548.

Crisp, D., Allen, D.A., Grinspoon, D.H., Pollack, J.B., 1991. The dark side of Venus: near-infrared images and spectra from the Anglo-Australian Observatory. Science 253, 1263–1266.

Crisp, D., Titov, D., 1997. The thermal balance of the Venus atmosphere. In: Bougher, S.W., Hunten, D.M., Philips, R.J. (Eds.), Venus II: Geology, Geophysics, Atmosphere, and Solar Wind Environment. University of Arizona Press, Tucson AZ, pp. 353–384.

D'Incecco, P., Muller, N., Helbert, J., D'Amore, M., 2017. Idunn Mons on Venus: location and extent of recently active lava flows. Planet. Space Sci. 136 https://doi.org/10.1016/j.pss.2016.12.002.

Dyar, M.D., Helbert, J., Boucher, T., Wendler, D., Walter, I., Widemann, T., Marcq, E., Maturilli, A., Ferrari, S., D'Amore, M., Muller, N., Smrekar, S., 2017. Mapping Venus mineralogy and chemistry in situ from orbit with six-window VNIR spectroscopy. 15th VEXAG. Abstract # 8004.

Eymet, V., 2008. KARINE: K-distribution atmospheric radiation & infrared net exchanges. Version 3.5.0. https://www.meso-star.com/projects/art/karine.html. (Accessed 16 September 2019).

Ford, J.P., Plaut, J.J., Weitz, C.M., Farr, T.G., Senske, D.A., Stofan, E.R., Michaels, G., Parker, T.J., 1993. Guide to magellan image interpretation. JPL Publication, 93-24.

Gilmore, M.S., Mueller, N., Helbert, J., 2015. VIRTIS emissivity of Alpha Regio, Venus, with implications for tessera composition. Icarus. https://doi.org/10.1016/j.icarus.2015.04.008.

Hashimoto, G.L., Imamura, T., 2001. Elucidating the rate of volcanism on Venus: detection of lava eruptions using Near-Infrared observations. Icarus 154. https://doi.org/10.1006/icar.2001.6713.

Hashimoto, G.L., Roos-Serote, M., Sugita, S., Gilmore, M.S., Kamp, L.W., Carlson, R.W., Baines, K.H., 2008. Felsic highland crust on Venus suggested by Galileo near-infrared mapping spectrometer data. J. Geophys. Res. 113 https://doi.org/10.1029/2008JE003134.

Haus, R., Arnold, G., 2010. Radiative transfer in the atmosphere of Venus and application to surface emissivity retrieval from VIRTIS/VEX measurements. Planet. Space Sci. 58.

Helbert, J., Maturilli, A., Dyar, M.D., Ferrari, S., Muller, N., Smrekar, S., 2017. First Set of Laboratory Venus Analog Spectra for All Atmospheric Windows. *48th LPSC*. Abstract #1512.

Helbert, J., Maturilli, A., Dyar, M.D., Ferrari, S., Muller, N., Smrekar, S., 2018. Orbital spectroscopy of the surface of Venus. 49th LPSC. Abstract #1512.

Herrick, R.R., Stahlke, D.L., Sharpton, V.L., 2012. Fine-scale Venusian topography from Magellan stereo data. Eos 93.

Jensen, J.R., 2007. Remote Sensing of the Environment: an Earth Resource Perspective, second ed. Prentice Hall, New Jersey.

Kappel, D., Arnold, G., Haus, R., 2016. Multi-spectrum retrieval of Venus IR surface emissivity maps from VIRTIS/VEX nightside measurements at Themis Regio. Icarus 265. https://doi.org/10.1016/j.icarus.2015.10.014.

Lebonnois, S., Eymet, V., Lee, C., d'Ollone, J.V., 2015. Analysis of the radiative budget of the Venusian atmosphere based on infrared Net Exchange Rate formalism. J. Geophys. Res.: Planets 120. https://doi.org/10.1002/2015JE004794.

Lillesand, T.M., Kiefer, R.W., Chipman, J.W., 2015. Remote Sensing and Image Interpretation. Wiley, New Jersey.

McGouldrick, K., Momary, T.W., Baines, K.H., Grinspoon, D.H., 2012. Quantification of middle and lower cloud variability and mesoscale dynamics from Venus Express/VIRTIS observations at 1.74 μm. Icarus 217. https://doi.org/10.1016/j.icarus.2011.07.009.

Moroz, V.I., Ekonomov, A.P., Moshkin, B.E., Revercomb, H.E., Sromovsky, L.A., Schofield, J.T., Spankuch, D., Taylor, F.W., Tomasko, M.G., 1985. Solar and thermal radiation in the Venus atmosphere. Adv. Space Res. 5 https://doi.org/10.1016/0273-1177(85)90202-9.

Moroz, V.I., 2002. Estimates of visibility of the surface of Venus from descent probes and balloons. Planet. Space Sci. 50.

Mueller, N., Helbert, J., Hashimoto, G.L., Tsang, C.C.C., Erard, S., Piccioni, G., Drossart, P., 2008. Venus surface thermal emission at 1 μm in VIRTIS imaging observations: evidence for variation of crust and mantle differentiation conditions. J. Geophys. Res. Lett. 113 https://doi.org/10.1029/2008JE003118.

Peralta, J., Lee, Y.J., McGouldrick, K., Sagawa, H., Sanchez-Lavega, A., Imamura, T., Widemann, T., Nakamura, M., 2017. Overview of useful spectral regions for Venus: an update to encourage observations complementary to the Akatsuki mission. Icarus 288. https://doi.org/10.1016/j.icarus.2017.01.027.

Pieters, C.M., Head, J.W., Patterson, W., Pratt, S., Garvin, J., Barsukov, V.L., Basilevsky, A.T., Khodakovsky, I.L., Selivanov, A.S., Panfilov, A.S., Gektin, Yu M., Narayeva, Y.M., 1986. The color of the surface of Venus. Science 234.

Rothman, L.S., Gordon, I.E., Barber, R.J., Dothe, H., Gamache, R.R., Goldman, A., Perevalov, V.I., Tashkun, S.A., Tennyson, J., 2010. HITEMP, the high-temperature molecular spectroscopic database. Journal of Quantitative Spectroscopy & Radiative Transfer 111. https://doi.org/10.1016/j.jqsrt.2010.05.001. In press.

Schlapfer, D., Richter, R., Hueni, A., 2009. "Recent developments in operational atmospheric and radiometric correction of hyperspectral imagery." Earsel SIG-IS Workshop. Tel. Aviv. https://doi.org/10.5167/uzh-24011.

Seiff, A., Schofield, J.T., Kliore, A.J., Taylor, F.W., Limaye, S.S., Revercomb, H.E., Sromovsky, L.A., Kerzhanovich, V.V., Moroz, V.I., Marov, M. Ya, 1985. Models of the structure of the atmosphere of Venus from the surface to 100 kilometers altitude. Adv. Space Res. 5.

Shalygin, E.V., Markiewicz, W.J., Basilevsky, A.T., Titov, D.V., Ignatiev, N.I., Head, J.W., 2015. Active volcanism on Venus in the Ganiki Chasma rift zone. Geophys. Res. Lett. 42 https://doi.org/10.1002/2015GL064088.

Smrekar, S.E., Stofan, E.R., Mueller, N., Treiman, A., Elkins-Tanton, L., Helbert, J., Piccioni, G., Drossart, P., 2010. Recent hotspot volcanism on Venus from VIRTIS emissivity data. Science 328. https://doi.org/10.1126/science.1186785.

Taylor, F.W., Crisp, D., Bezard, B., 1997. Near-Infrared sounding of the lower atmosphere of Venus. In: Bougher, S.W., Hunten, D.M., Philips, R.J. (Eds.), Venus II: Geology, Geophysics, Atmosphere, and Solar Wind Environment. University of Arizona Press, Tucson AZ, pp. 325–351.

Titov, D.V., Bullock, M.A., Crisp, D., Renno, N.O., Taylor, F.W., Zasova, L.V., 2007. Radiation in the atmosphere of Venus. In: Esposito, L.W., Stofan, E.R., Cravens, T.E. (Eds.), Exploring Venus as a Terrestrial Planet. American Geophysical Union, Washington, D.C., pp. 7–22. https://doi.org/10.1029/176GM08

Treiman, A.H., 2007. "Geochemistry of Venus' surface: current limitations as future opportunities. In: Esposito, L.W., Stofan, E.R., Cravens, T.E. (Eds.), Exploring Venus as a Terrestrial Planet. American Geophysical Union, Washington, D.C., pp. 7–22. https://doi.org/10.1029/176GM01

Williams, D.R.. "Visible and infrared thermal imaging spectrometer (VIRTIS)." *NASA space science data coordinated archive*. https://nssdc.gsfc.nasa.gov/nmc/experiment/display.action?id=2005-045A-02. (Accessed 1 October 2019).